SULoRA: Subspace Unmixing With Low-Rank Attribute Embedding for Hyperspectral Data Analysis

Danfeng Hong, *Student Member, IEEE*, and Xiao Xiang Zhu, *Senior Member, IEEE*

***Abstract*—To support high-level analysis of spaceborne imaging spectroscopy (hyperspectral) imagery, spectral unmixing has been gaining significance in recent years. However, from the inevitable spectral variability, caused by illumination and topography change, atmospheric effects and so on make it difficult to accurately estimate abundance maps in spectral unmixing. Classical unmixing methods, e.g., linear mixing model (LMM) and extended LMM, fail to robustly handle this issue, particularly facing complex spectral variability. To this end, we propose a subspace-based unmixing model using low-rank learning strategy, called subspace unmixing with low-rank attribute embedding (SULoRA), robustly against spectral variability in inverse problems of hyperspectral unmixing. Unlike those previous approaches that unmix the spectral signatures directly in original space, SULoRA is a general subspace unmixing framework that jointly estimates subspace projections and abundance maps in order to find a raw subspace that is more suitable for carrying out the unmixing procedure. More importantly, we model such raw subspace with low-rank attribute embedding. By projecting the original data into a low-rank subspace, SULoRA can effectively address various spectral variabilities in spectral unmixing. Furthermore, we adopt an alternating direction method of multipliers based algorithm to solve the resulting optimization problem. Extensive experiments on synthetic and real datasets are performed to demonstrate the superiority and effectiveness of the proposed method in comparison with the previous state-of-the-art methods.**

***Index Terms*—Alternating direction method of multipliers, hyperspectral data analysis, low-rank attribute embedding, remote sensing, subspace unmixing, spectral variability.**

I. Introduction

HYPERSPECTRAL imagery (HSI) is characterized by very rich spectral information, which enables us to detect targets of interest and identify unknown materials more easily. Motivated by this, considerable attentions have been paid to hyperspectral data processing and analysis, such as dimensionality reduction [1], [2], image segmentation [3], land-cover and land-use classification [4], and target detection [5] and so on. However, most of pixels in HSI suffer from the effect of spectral mixing due to a lower spatial-resolution than that of traditional RGB or multispectral imagery. These material mixtures inevitably degrade the spectrally discriminative ability, particularly in some high-level applications. To overcome this, spectral unmixing is defined as that decomposes the reference spectral signatures into a collection of spectral signatures of pure materials (or *endmembers*) and their abundance fractions (or *abundance maps*). In remote sensing community, spectral unmixing techniques have been widely and successfully applied to a variety of tasks, including mineral exploration and identification [6], forest monitoring [7].

Assuming the absent of any spectral, spatial, and temporal variabilities as well as microscopic interaction (e.g. multiple scatting, intimate mixing, etc.) between the materials are negligible, then the mixed spectrum of each pixel in the HSI scene is approximately measured by a *linear mixing model* (LMM) [8]. There is, however, a main factor-spectral variability, propagating unpredictable errors to LMM. This further yields an inaccurate unmixing process, since these errors are basically absorbed by *endmembers* and *abundance maps*. Nonlinearity, i.e. nonlinearly mixing spectral signatures, resulting from, e.g. multiple scattering and intimate mixing, is one of the main causes of spectral variability. In addition, varying acquisition conditions (e.g. illumination, topography, atmospheric effects) as well as physically and chemically intrinsic change of the material possibly speed up spectral degradation, which can be seen as another kind of spectral variability.

Recently, enormous efforts modeling errors either from statistics-based or regression-based point of view have been made to address the spectral variability [9]. Two mainstream statistical methods, namely the normal composition model [10] and the beta compositional model [11], assume the endmember spectra following a given probability distribution. On the other hand, inspired by LMM-the regression-based seminal work, and its variations have been successively proposed to deterministically model the spectral variability. A perturbed linear mixing model (PLMM) was proposed in [12] to fit the spectral variability using a Gaussian prior with each endmember. Similarly, Fu *et al.* designed a dictionary-adjusted nonconvex sparsity-encouraging regression (DANSER) by modeling the mismatch between the spectral library and the observed spectrum under a Gaussian distribution [13]. Although these approaches attempt to model the spectral variability in a general way, only a given explicit distribution, i.e. Gaussian, is still insufficient. In most

Manuscript received April 15, 2018; revised August 9, 2018; accepted September 4, 2018. Date of publication October 22, 2018; date of current version December 17, 2018. This work was supported in part by the European Research Council under the European Union's Horizon 2020 research and innovation programme under Grant ERC-2016-StG-714087 and in part by the Helmholtz Association under the framework of the Young Investigators Group "SiPEO" (VH-NG-1018, www.sipeo.bgu.tum.de). The guest editor coordinating the review of this paper and approving it for publication was Prof. Thierry Bouwmans. *(Corresponding author: Xiao Xiang Zhu.)*

The authors are with the Remote Sensing Technology Institute (IMF), German Aerospace Center (DLR), Wessling 82234, Germany, and also with the Signal Processing in Earth Observation, Technical University of Munich, Munich 80333, Germany (e-mail: danfeng.hong@dlr.de; xiao.zhu@dlr.de).

Color versions of one or more of the figures in this paper are available online at http://ieeexplore.ieee.org.

Digital Object Identifier 10.1109/JSTSP.2018.2877497

1932-4553 © 2018 IEEE. Translations and content mining are permitted for academic research only. Personal use is also permitted, but republication/redistribution requires IEEE permission. See http://www.ieee.org/publications_standards/publications/rights/index.html for more information.

hyperspectral scenes, the spectral signature is frequently scaled due to illumination or topological change, hence the scaling factor, as a principal variability, is quite coherent with the corresponding spectral signature. Such attributed spectral variability is hardly represented by a Gaussian-guided term. Drumetz *et al.* proposed an extended LMM (ELMM) [14] by modeling the different scaling factors on each endmember, but is a significant shortcoming in that other spectral variabilities are not be involved correspondingly.

While aforementioned unmixing algorithms have been successively proposed and successfully applied to some specific datasets, the ability of robustness and generalization in handling various spectral variabilities still remains limited. For this reason, we propose a robust subspace-based unmixing method by jointly performing subspace learning and unmixing in a closed-loop. With low-rank attribute embedding, the spectral variability can be effectively removed in the learnt low-rank subspace, achieving a robust spectral unmixing. More specifically, our contributions can be unfolded as follows:

- We propose a general subspace-based unmixing framework by jointly low-rank subspace learning and unmixing, called **s**ubspace **u**nmixing with **l**ow-**r**ank **a**ttribute embedding (SULoRA), to achieve a robust unmixing in a proper subspace rather than in the original space. Moreover, mostly linear unmixing models can be considered as special cases in this general framework.
- With the low-rank attribute embedding, the proposed SULoRA can broadly mitigate the effects of various spectral variabilities by projecting the original data into a more representative low-rank subspace.
- An alternating direction method of multipliers (ADMM) is adopted to solve the resulting optimization problem.

The remainder of this paper is organized as follows. Section II briefly summarizes the related work in spectral unmixing and analyzes their advantages and disadvantages. In Section III, we first clarify the motivation and then propose our methodology of the SULoRA model as well as corresponding ADMM-based optimization algorithm. Section IV presents the experimental results on two different datasets (a synthetic data and a real urban data) and gives the intuitive analysis and discussion both qualitatively and quantitatively. Finally, Section V concludes with a summary.

II. Related Work

In this section, we review state-of-arts unmixing algorithms, emphatically introducing LMM-based unmixing models and its variations including fully constrained least squares unmixing (FCLSU) [15], partial constrained least squares unmixing (PCLSU) [16], sparse unmixing by variable splitting and augmented Lagrangian (SUnSAL) [17], as well as their scaled versions (scaled partial constrained least squares unmixing (SPCLSU) [18] and scaled sparse unmixing by variable splitting and augmented Lagrangian (SSUnSAL) [19]), ELMM and PLMM.

A. LMM

Let $\mathbf{Y} = [\mathbf{y}_1, \ldots, \mathbf{y}_i, \ldots, \mathbf{y}_N] \in \mathbb{R}^{D\times N}$ be an unfolded HSI with D bands and N pixels, and $\mathbf{A} = [\mathbf{a}_1, \ldots, \mathbf{a}_P] \in \mathbb{R}^{D\times P}$ be the endmembers with the size of $D \times P$. $\mathbf{X} = [\mathbf{x}_1, \ldots, \mathbf{x}_i, \ldots, \mathbf{x}_N] \in \mathbb{R}^{P\times N}$ is denoted as abundance maps, whose each column vector stands for the fractional abundance at each pixel. $\mathbf{R} = [\mathbf{r}_1, \ldots, \mathbf{r}_i, \ldots, \mathbf{r}_N] \in \mathbb{R}^{D\times N}$ is the residual (e.g. noise, modeling errors and others) in the form of matrix. Under an ideal condition without any external disturbance, the spectral measurement for a given pixel, denoted by $\mathbf{y}_i \in \mathbb{R}^{D\times 1}$, is well approximated by a set of linear combination of endmember spectra weighted by theri corresponding fractional abundances, resulting in the LMM:

$$\mathbf{y}_i = \mathbf{A}\mathbf{x}_i + \mathbf{r}_i, \tag{1}$$

where $\mathbf{a}_i$ and $\mathbf{x}_i$ should be non-negative in order to meet the physical conditions in reality. Moreover, the fractional abundance $\mathbf{x}_i$, as the name indicated, represents the proportions occupied by the different endmembers. This means $\mathbf{x}_i$ should be also subject to a sum-to-one constraint. Therefore, Eq. (1) with the necessary constraints is expressed as

$$\mathbf{y}_i = \mathbf{A}\mathbf{x}_i + \mathbf{r}_i, \quad \text{s.t. } \mathbf{A} \succeq \mathbf{0},\ \mathbf{x}_i \succeq 0,\ \sum_{i=1}^{N} \mathbf{x}_i = 1. \tag{2}$$

Collecting all pixels, a compact matrix form of Eq. (2) can be written as

$$\mathbf{Y} = \mathbf{A}\mathbf{X} + \mathbf{R}, \quad \text{s.t. } \mathbf{A} \succeq \mathbf{0},\ \mathbf{X} \succeq \mathbf{0},\ \mathbf{1}^{\mathrm{T}}\mathbf{X} = \mathbf{1}. \tag{3}$$

In the following, we will detail several popular unmixing algorithms based on LMM:

1) FCLSU: In practice, the endmembers ($\mathbf{A}$) can be pre-extracted from the given scene using endmember extraction methods, i.e. pixel purity index (PPI), vertex component analysis (VCA) [20]. This renders us to more effectively and conveniently estimate the abundance maps ($\mathbf{X}$) by degrading the Eq. (3) to least-square regression problem, leading to FCLSU:

$$\min_{\mathbf{X}} \left\{ \frac{1}{2}\|\mathbf{Y} - \mathbf{A}\mathbf{X}\|_{\mathrm{F}}^2 \quad \text{s.t. } \mathbf{X} \succeq \mathbf{0},\ \mathbf{1}^{\mathrm{T}}\mathbf{X} = \mathbf{1}. \right\}. \tag{4}$$

Considering the presence of spectral variability, FCLSU yields a poor performance. It mainly derives from the strong sum-to-constraint, as explained in [8]. A common way to this issue is to relax the abundance fractions sum to less or larger than one or to consider a part of full constraints.

2) PCLSU: Following the above solution, the resulting PCLSU can be formulated by solving

$$\min_{\mathbf{X}} \left\{ \frac{1}{2}\|\mathbf{Y} - \mathbf{A}\mathbf{X}\|_{\mathrm{F}}^2 \quad \text{s.t. } \mathbf{X} \succeq \mathbf{0}. \right\}. \tag{5}$$

The estimated variable $\mathbf{X}$ in Eq. (5) might be any scales, owing to a badly-conditioned observed matrix $\mathbf{Y}$. To alleviate the effects of the ill-posed problem, meaningfully physical assumptions have to be added in the form of regularization.

3) SUnSAL: As observed, the abundances on each endmember are theoretically supposed to be sparse. Bioucas-Dias *et al.* embedded this property into LMM and achieved a powerful SUnSAL algorithm. The resulting optimization problem can be

written as follows

$$\min_{\mathbf{X}} \left\{ \frac{1}{2}\|\mathbf{Y}-\mathbf{A}\mathbf{X}\|_{\mathrm{F}}^2 + \alpha\|\mathbf{X}\|_{1,1} \text{ s.t. } \mathbf{X}\succeq\mathbf{0},\ \mathbf{1}^{\mathrm{T}}\mathbf{X}=\mathbf{1}. \right\}, \tag{6}$$

where $\|\mathbf{X}\|_{1,1} \equiv \sum_{k=1}^{N}\|\mathbf{x}_k\|_1$ is denoted as an approximation of sparsity-promoting term.

In view of effectiveness of SUnSAL, SUnSAL's variations have been subsequently proposed in recent years, such as SUnSAL with total variation spatial regularization (SUnSAL-TV) [21], collaborative sparse regression (CLSUnSAL) [22], etc. We have to admit, however, that these advanced methods are still subject to the framework of LMM that is sensitive to spectral variabilities.

B. ELMM

ELMM aims to modeling the principle spectral variability (scaling factors) to allow a pixel-wise variation at each endmember:

$$\mathbf{y}_i = \mathbf{A}\mathbf{S}_i\mathbf{x}_i + \mathbf{r}_i, \tag{7}$$

where $\mathbf{S}_i \in \mathbb{R}^{P\times P}$ is a diagonal matrix with the nonnegative constraint ($\mathbf{S}_i \succeq 0$). A matrix form of Eq. (7) can be repented as

$$\mathbf{Y} = \mathbf{A}(\mathbf{S}\odot\mathbf{X}) + \mathbf{R}, \tag{8}$$

here $\mathbf{S}\in\mathbb{R}^{P\times N}$ is a full matrix collecting the scaling factors from all pixels whose i^{th} column is $\mathbf{S}_i$. The operator $\odot$ is denoted as the Schur-Hadamard (termwise) product.

1) Unmixing Under the ELMM: Intuitively, the optimization problems in (7) and (8) are hardly to be analytically solved. In [14], a trick is employed by splitting the coupled variables ($\mathbf{S}$ and $\mathbf{X}$), then we have

$$\min_{\mathbf{X},\mathbf{S}\succeq 0,\underline{\mathbf{A}}} \left\{ \sum_{k=1}^{N} \left(\|\mathbf{y}_k - \mathbf{A}_k\mathbf{x}_k\|_2^2 + \lambda_S\|\mathbf{A}_k - \mathbf{A}_0\mathbf{S}_k\|_{\mathrm{F}}^2 \right) \right\}, \tag{9}$$

where $\mathbf{A}_0$ is the reference endmember spectrum, $\underline{\mathbf{A}} = \{\mathbf{A}_i\}$ is a collection of pixel-dependent endmember matrices, and λ_S plays a balance role between the two separated terms. Eq. (9) can be alternatively optimized with respect to each variable by alternating minimization strategy [23].

2) SPCLSU: Prior to ELMM, scaling factors have been investigated in a simple way, that is SPCLSU [18] in which endmembers are reasonably assumed by sharing a same scale as the scaling factors are strongly associated with topography. SPCLSU actually conducts a PCLSU in the beginning, and then normalizes the abundance maps to meet sum-to-one. This is a simple but effective strategy, which is also involved in our proposed method.

C. PLMM

As the name suggested, PLMM attempts to describe the spectral variability as an additive perturbation information. Both the pixel-wise and the corresponding matrix form of PLMM can be expressed, respectively

$$\mathbf{y}_i = (\mathbf{A}+\mathbf{\Delta}_i)\mathbf{x}_i + \mathbf{r}_i, \tag{10}$$

and

$$\mathbf{Y} = \mathbf{A}\mathbf{X} + \underbrace{[\mathbf{\Delta}_1\mathbf{x}_1|\ldots|\mathbf{\Delta}_i\mathbf{x}_i|\ldots|\mathbf{\Delta}_N\mathbf{x}_N]}_{\mathbf{\Delta}} + \mathbf{R}, \tag{11}$$

where $\mathbf{\Delta}$ is $[\mathbf{\Delta}_1\mathbf{x}_1|\ldots|\mathbf{\Delta}_i\mathbf{x}_i|\ldots|\mathbf{\Delta}_N\mathbf{x}_N]$ denotes the perturbation information of the endmembers.

1) Unmixing Under the PLMM: The optimization problem corresponding to PLMM-based unmixing can be given as

$$\min_{\mathbf{A},\mathbf{\Delta},\mathbf{X}} \left\{ \begin{array}{l} \frac{1}{2}\|\mathbf{Y}-\mathbf{A}\mathbf{X}-\mathbf{\Delta}\|_{\mathrm{F}}^2 + \alpha\mathbf{\Phi}(\mathbf{X}) + \beta\mathbf{\Psi}(\mathbf{A}) \\ +\gamma\mathbf{\Upsilon}(\mathbf{\Delta}) \end{array} \right\}, \tag{12}$$

where $\mathbf{\Phi}$, $\mathbf{\Psi}$, and $\mathbf{\Upsilon}$ parameterized by α, β, and γ, are penalties with respect to variables $\mathbf{X}$, $\mathbf{A}$, and $\mathbf{\Delta}$, receptively. Notably, $\mathbf{\Upsilon}$ term is modeled by a Frobenius norm.

2) DANSER: Likewise being generalized to PLMM framework, DANSER adopts a sparsity-encouraging regression technique for a dictionary-based spectral unmixing, where a perturbation-like information is explored to measure the mismatch between spectral dictionary and observed endmembers. This model, the DANSER, is formulated by

$$\min_{\mathbf{A}',\mathbf{X}} \left\{ \begin{array}{l} \frac{1}{2}\|\mathbf{Y}-\mathbf{A}'\mathbf{X}\|_{\mathrm{F}}^2 + \alpha\|\mathbf{A}'-\mathbf{A}\|_{\mathrm{F}}^2 + \beta\|\mathbf{X}\|_{2,p}^p \\ \text{s.t. } \mathbf{X}\succeq\mathbf{0} \end{array} \right\}, \tag{13}$$

where $\mathbf{A}'$ is a corrupted endmember matrix obtained by perturbing $\mathbf{A}$.

Although the aforementioned methods have shown an advancement in treating the spectral variability, especially facing main spectral variabilities (e.g. scaling factors), they are still lack of robustness and generalization to others that we are unknown. Jump out of this circle, a new insight is provided into this problem that we propose to conduct the spectral unmixing in a robust subspace instead of directly unmixing in original spectral space. Please go to next section for more details.

III. Subspace Unmixing With Low-Rank Attribute Embedding

A. General Motivation

There is a trade-off between spectral information gain and the spectral variability. On one hand, spectrum are expected to be spectrally discriminative. Conversely, this means that more complex spectral variabilities might get involved in hyperspectral data. A feasible solution to this issue is spectral unmixing in a 'raw' subspace rather than in the original space. In the learnt subspace, the pixels belonging to the same class are expected to be strongly correlated by using a low-rank attribute embedding. Further, this process can be mathematically modeled as

$$\begin{aligned} &\mathbf{Y} = \mathbf{Y}' + \mathbf{R}',\ \text{s.t. } \mathbf{Y}' = \mathbf{\Theta}\mathbf{Y}, \\ &\mathbf{Y}' = \mathbf{\Theta}\mathbf{A}\mathbf{X} + \mathbf{R}'', \end{aligned} \tag{14}$$

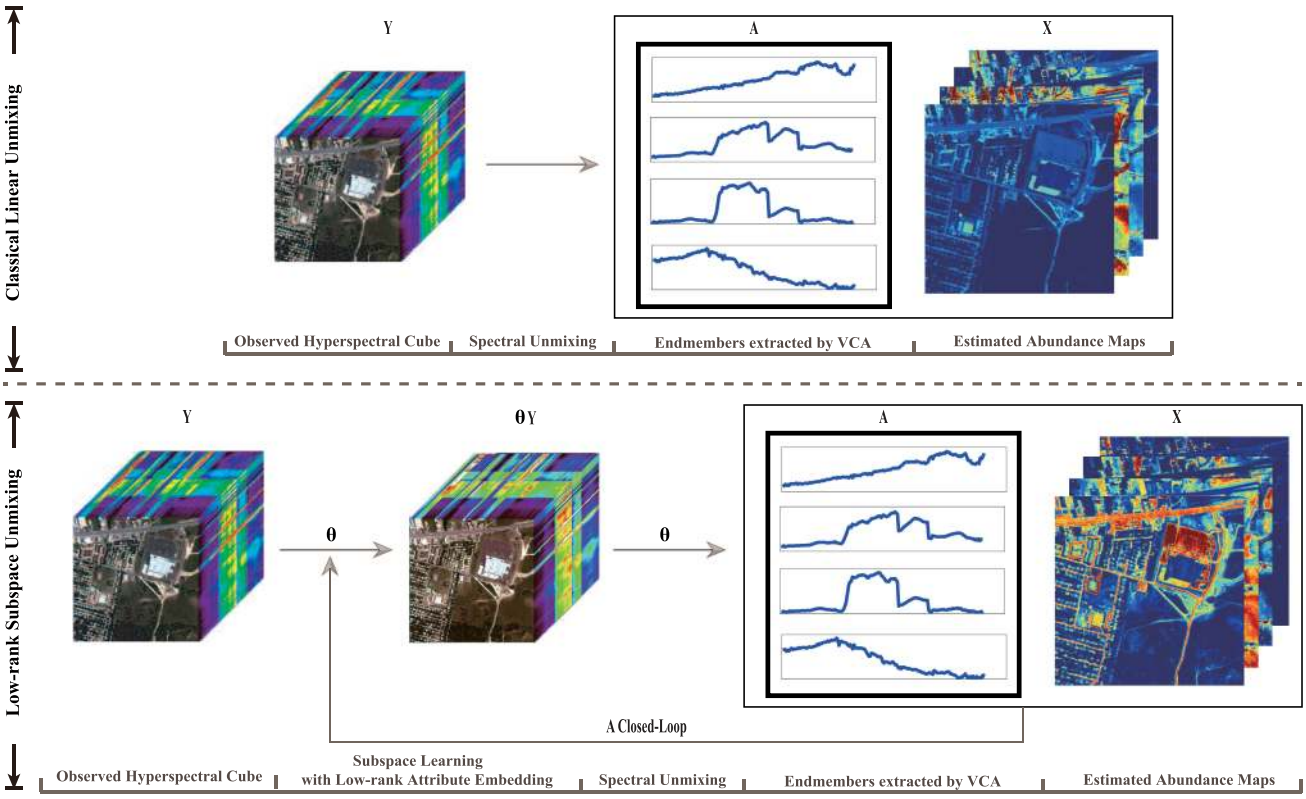

Fig. 1. A comparison of the holistic workflow between the original-space-based method and the proposed SULoRA.

where $\mathbf{\Theta}$ denotes the low-rank subspace projections, and $\mathbf{Y}'$ is the spectrally subspace representation after embedding the low-rank attribute.

Fig. 1 shows a comparison in holistic workflow of spectral unmixing between using the original-space-based and the subspace-based (SULoRA) approaches.

B. Low-Rank Attribute Embedding

Inspired by [24] in which a novel strategy of low-rank attribute embedding is proposed with the application to person re-identification, we further improve this term by integrating our general motivation described above, making it more applicable to hyperspectral unmixing task.

Step by step, we will clarify the motivation of using the low-rank attribute embedding in great detail. It is well-known that hyperspectral imagery inevitably suffers from various spectral variabilities in the process of imaging. These spectral variabilities, which are generated due to illumination conditions, topography change, atmospheric effects, and material nonlinear mixing, are complex and even hardly represented using a common model. Instead of directly modeling such changeable property, we hypothetically treat the spectral variability as *an unknown complex noise*. Therefore, modeling the complex spectral variability could be converted to a special denoising problem. Noises in the data can be generally removed through a projection transformation. During this process, one is expected to be the projected or denoised data as close as possible with the original data, resulting in a mathematical expression ($\mathbf{Y} \doteq \mathbf{\Theta Y}$). Besides, we also expect to structurally maintain consistency between noisy data ($\mathbf{Y}$) and processed data ($\mathbf{\Theta Y}$), which might be achieved by correlative or collaborative filtering in order to emphasize the correlation and structural property between the samples. Low-rank representation has been widely and successfully applied for modeling the sample-based correlation [25]–[27], hence the estimated projection $\mathbf{\Theta}$ can be naturally endowed with a low-rank attribute (e.g., rank $(\mathbf{\Theta}) \preceq C$) in our case.

C. Problem Formulation

As introduced in Subsection III-A, our proposed SULoRA shown in Eq. (14) can be formulated as a following constrained optimization problem

$$\min_{\mathbf{X},\mathbf{\Theta}} \left\{ \begin{array}{l} \frac{1}{2}\|\mathbf{\Theta}(\mathbf{Y}-\mathbf{AX})\|_{\mathrm{F}}^2 + \Phi(\mathbf{\Theta}) + \Upsilon(\mathbf{X}) \\ \quad \text{s.t. } \mathbf{X} \succeq \mathbf{0} \end{array} \right\}, \tag{15}$$

which aims at estimating the variables with respect to $\mathbf{X}$ and $\mathbf{\Theta}$. Since the problem (15) is undetermined, the variables $\mathbf{X}$ and $\mathbf{\Theta}$ should be regularized by reasonable prior knowledge. The two regularization terms $\Phi(\mathbf{\Theta})$ and $\Upsilon(\mathbf{X})$ are described below.

1) Subspace Regularization $\Phi(\mathbf{\Theta})$*:* According to the discussion and analysis in Section III-B, the subspace projections $\mathbf{\Theta}$ are characterized by a low-rank attribute in order to transfer the original hyperspectral data into a robust subspace, which can be approximately formulated by the form of $\|\mathbf{\Theta}\|_*$. Essentially, the main difference between those previously proposed low-rank representation learning and the proposed SULoRA lies in

the motive. More specifically, the former ones usually aim to robust clustering in subspace [25], [27] that needs to estimate the connectivity between samples, while our goal is to find or learn a low-rank subspace projection so that the learned projection can play a correlative filtering-like role robustly against various spectral variabilities, which is computationally efficient. Besides, we also hope to structurally maintain the spectral properties, making the learnt subspace as close as possible with the original space. This second prior can be formed by $\|\mathbf{Y}-\mathbf{\Theta Y}\|_F$. The final resulting expression of regularization with respect to $\mathbf{\Theta}$ is

$$\Phi(\mathbf{\Theta})=\frac{\alpha}{2}\|\mathbf{Y}-\mathbf{\Theta Y}\|_{\mathrm{F}}^2+\beta\|\mathbf{\Theta}\|_*, \tag{16}$$

where α and β are the corresponding penalty parameters.

2) Abundance Regularization $\Upsilon(\mathbf{X})$: For a given hyperspectral scene, the spectral signature consists of limited kinds of materials, hence the abundances should be encouraged to be sparse. This term parameterized by γ can be expressed by

$$\Upsilon(\mathbf{X})=\gamma\|\mathbf{X}\|_{1,1}. \tag{17}$$

In our model, the non-negativity constraint ($\mathbf{X}\succeq\mathbf{0}$) has to be considered to satisfy the physical assumption. It should be noted, however, that the sum-to-one constraint is not directly considered in our optimization problem (Eq. (15)), since the hard constraint is too strong to yield a badly-estimated abundance maps. We adopt the same technique in SPCLSU [18] to force $\mathbf{X}$ to follow the sum-to-one constraint.

Different with matrix factorization-based unmixing approaches that simultaneously estimate the endmembers and the abundance maps, the proposed SULoRA first determines the number of endmembers via HySime [28], and then separately extracts the endmembers from the HSI scene with VCA and estimates the abundance maps. The benefits of the scheme in our model are two-fold. On one hand, the endmembers extracted from the data tend to preserve, to the greatest extent, spectrally physical significance, and thereby improve the stability of estimating the abundance maps. On the other hand, it effectively simplifies the model's complexity by optimizing fewer variables, finding a good solution easier.

D. Model Optimization Using ADMM-Based Algorithm

The optimization problem shown in Eq. (15) is convex, we adopt an ADMM-based optimization algorithm [29]–[31] for a fast and efficient solution. To facilitate the use of ADMM, we first convert Eq. (15) to an equivalent form introducing multiple auxiliary variables $\mathbf{G}$, $\mathbf{H}$, and $\mathbf{J}$ to replace $\mathbf{\Theta}$, $\mathbf{X}$, and $\mathbf{X}$, respectively.

$$\min_{\mathbf{X},\mathbf{\Theta},\mathbf{G},\mathbf{H},\mathbf{J}}\left\{\begin{array}{l}\dfrac{1}{2}\|\mathbf{\Theta}(\mathbf{Y}-\mathbf{AX})\|_{\mathrm{F}}^2+\dfrac{\alpha}{2}\|\mathbf{Y}-\mathbf{\Theta Y}\|_{\mathrm{F}}^2\\ +\beta\|\mathbf{G}\|_*+\gamma\|\mathbf{H}\|_{1,1}+l_R^+(\mathbf{J})\\ \text{s.t. }\mathbf{\Theta}=\mathbf{G},\ \mathbf{X}=\mathbf{H},\ \mathbf{X}=\mathbf{J}\end{array}\right\}, \tag{18}$$

where $()^+$ denotes an operator that intercepts the positive part of each component of the matrix, and $l_R^+(\mathbf{J})$ is defined as $\mathbf{J}\succeq\mathbf{0}$. This problem can be equivalently solved by minimizing the following augmented Lagrangian function:

$$\begin{aligned}\mathscr{L}_U(\mathbf{X},\mathbf{\Theta},\mathbf{G},\mathbf{H},\mathbf{J},\mathbf{\Lambda}_1,\mathbf{\Lambda}_2,\mathbf{\Lambda}_3)&=\frac{1}{2}\|\mathbf{\Theta}(\mathbf{Y}-\mathbf{AX})\|_{\mathrm{F}}^2\\&+\frac{\alpha}{2}\|\mathbf{Y}-\mathbf{\Theta Y}\|_{\mathrm{F}}^2+\beta\|\mathbf{G}\|_*+\gamma\|\mathbf{H}\|_{1,1}+l_R^+(\mathbf{J})\\&+\mathbf{\Lambda}_1^{\mathrm{T}}(\mathbf{G}-\mathbf{\Theta})+\mathbf{\Lambda}_2^{\mathrm{T}}(\mathbf{H}-\mathbf{X})+\mathbf{\Lambda}_3^{\mathrm{T}}(\mathbf{J}-\mathbf{X})\\&+\frac{\mu}{2}\|\mathbf{G}-\mathbf{\Theta}\|_{\mathrm{F}}^2+\frac{\mu}{2}\|\mathbf{H}-\mathbf{X}\|_{\mathrm{F}}^2+\frac{\mu}{2}\|\mathbf{J}-\mathbf{X}\|_{\mathrm{F}}^2,\end{aligned} \tag{19}$$

where $\{\mathbf{\Lambda_i}\}_{i=1}^3$ are Lagrange multipliers and μ is the penalty parameter. The specific optimization flow for solving the problem (19) is summarized in Algorithm 1, and the solution to each subproblem is detailed in the following.

Algorithm 1: Subspace Unmixing With Low-Rank Attribute Embedding (SULoRA).

Input: $\mathbf{Y}$, $\mathbf{A}$, $\mathbf{X}_0$, α, β, γ, $maxIter$.
Output: $\mathbf{X}$, $\mathbf{\Theta}$.

Initialization: $\mathbf{G}=\mathbf{0}$, $\mathbf{H}=\mathbf{0}$, $\mathbf{J}=\mathbf{0}$, $\mathbf{\Lambda}_1=\mathbf{0}$, $\mathbf{\Lambda}_2=\mathbf{0}$, $\mathbf{\Lambda}_3=\mathbf{0}$, $\mu=10^{-3}$, $\mu_m=10^6$, $\rho=1.5$, $\varepsilon=10^{-6}$, $t=1$.
while *not converged* or $t>maxIter$ **do**
  Fix other variables to update $\mathbf{\Theta}$ by
  $$\mathbf{\Theta}=(\alpha\mathbf{YY}^{\mathrm{T}}+\mu\mathbf{G}+\mathbf{\Lambda}_1)\times(\alpha\mathbf{YY}^{\mathrm{T}}+(\mathbf{Y}-\mathbf{AX})(\mathbf{Y}-\mathbf{AX})^{\mathrm{T}}+\mu\mathbf{I})^{-1}.$$
  Fix other variables to update $\mathbf{X}$ by
  $$\mathbf{X}=((\mathbf{\Theta A})^{\mathrm{T}}(\mathbf{\Theta A})+2\mu\mathbf{I})^{-1}\times((\mathbf{\Theta A})^{\mathrm{T}}\mathbf{\Theta Y}+\mu\mathbf{H}+\mathbf{\Lambda}_2+\mu\mathbf{J}+\mathbf{\Lambda}_3).$$
  Fix other variables to update $\mathbf{G}$ by
  $$[\mathbf{U},\mathbf{S},\mathbf{V}]=\mathrm{svd}(\mathbf{\Theta}-\mathbf{\Lambda}_1/\mu),\quad \mathbf{S}=\mathrm{diag}(\{s_k\}_{k=1}^r)$$
  $$\mathbf{G}=\mathbf{US}_\tau\mathbf{V},\quad \mathbf{S}_\tau=\mathrm{diag}(\max\{0,s_k-\beta/\mu\}).$$
  Fix other variables to update $\mathbf{H}$ by
  $$\mathbf{H}=\max\{\mathbf{0},|\mathbf{X}-\mathbf{\Lambda}_2/\mu|-\gamma/\mu\}\odot sign(\mathbf{X}-\mathbf{\Lambda}_2/\mu).$$
  Fix other variables to update $\mathbf{J}$ by
  $$\mathbf{J}=\max\{\mathbf{0},\mathbf{X}-\mathbf{\Lambda}_3/\mu\}.$$
  Update Lagrange multipliers by
  $$\mathbf{\Lambda}_1\leftarrow\mathbf{\Lambda}_1+\mu(\mathbf{G}-\mathbf{\Theta}),\ \mathbf{\Lambda}_2\leftarrow\mathbf{\Lambda}_2+\mu(\mathbf{H}-\mathbf{X})$$
  $$\mathbf{\Lambda}_3\leftarrow\mathbf{\Lambda}_3+\mu(\mathbf{J}-\mathbf{X}).$$
  Update penalty parameter by
  $$\mu=\min(\rho\mu,\mu_m).$$
  Check the convergence conditions: **if** $\|\mathbf{G}-\mathbf{\Theta}\|_{\mathrm{F}}<\varepsilon$ *and* $\|\mathbf{G}-\mathbf{X}\|_{\mathrm{F}}<\varepsilon$ *and* $\|\mathbf{J}-\mathbf{X}\|_{\mathrm{F}}<\varepsilon$ **then**
    Stop iteration;
  else
    $t\leftarrow t+1$;
  end
end

We successively minimize $\mathscr{L}_U$ with respect to the variables $\mathbf{\Theta}$, $\mathbf{X}$, $\mathbf{G}$, $\mathbf{H}$, and $\mathbf{J}$ as well as Lagrange multipliers $\{\mathbf{\Lambda_i}\}_{i=1}^3$ as follows:

Optimization with respect to $\mathbf{\Theta}$*:* The optimization problem for $\mathbf{\Theta}$ is

$$\min_{\mathbf{\Theta}} \left\{ \begin{array}{l} \frac{1}{2}\|\mathbf{\Theta}(\mathbf{Y}-\mathbf{A}\mathbf{X})\|_{\mathrm{F}}^2 + \frac{\alpha}{2}\|\mathbf{Y}-\mathbf{\Theta}\mathbf{Y}\|_{\mathrm{F}}^2 \\ \quad + \mathbf{\Lambda}_1^{\mathrm{T}}(\mathbf{G}-\mathbf{\Theta}) + \frac{\mu}{2}\|\mathbf{G}-\mathbf{\Theta}\|_{\mathrm{F}}^2 \end{array} \right\}, \tag{20}$$

which has an analytical solution of

$$\begin{aligned} \mathbf{\Theta} \leftarrow\ & (\alpha\mathbf{Y}\mathbf{Y}^{\mathrm{T}} + \mu\mathbf{G} + \mathbf{\Lambda}_1) \\ & \times (\alpha\mathbf{Y}\mathbf{Y}^{\mathrm{T}} + (\mathbf{Y}-\mathbf{A}\mathbf{X})(\mathbf{Y}-\mathbf{A}\mathbf{X})^{\mathrm{T}} + \mu\mathbf{I})^{-1}. \end{aligned} \tag{21}$$

Optimization with respect to $\mathbf{X}$*:* For $\mathbf{X}$, the optimization problem can be expressed as

$$\min_{\mathbf{X}} \left\{ \begin{array}{l} \frac{1}{2}\|\mathbf{\Theta}(\mathbf{Y}-\mathbf{A}\mathbf{X})\|_{\mathrm{F}}^2 + \mathbf{\Lambda}_2^{\mathrm{T}}(\mathbf{H}-\mathbf{X}) + \mathbf{\Lambda}_3^{\mathrm{T}}(\mathbf{J}-\mathbf{X}) \\ \quad + \frac{\mu}{2}\|\mathbf{H}-\mathbf{X}\|_{\mathrm{F}}^2 + \frac{\mu}{2}\|\mathbf{J}-\mathbf{X}\|_{\mathrm{F}}^2 \end{array} \right\}, \tag{22}$$

whose a closed-form solution is

$$\begin{aligned} \mathbf{X} \leftarrow\ & ((\mathbf{\Theta}\mathbf{A})^{\mathrm{T}}(\mathbf{\Theta}\mathbf{A}) + 2\mu\mathbf{I})^{-1} \\ & \times ((\mathbf{\Theta}\mathbf{A})^{\mathrm{T}}\mathbf{\Theta}\mathbf{Y} + \mu\mathbf{H} + \mathbf{\Lambda}_2 + \mu\mathbf{J} + \mathbf{\Lambda}_3). \end{aligned} \tag{23}$$

Optimization with respect to $\mathbf{G}$*:* The objective function for $\mathbf{G}$ is written as

$$\min_{\mathbf{G}} \left\{ \beta\|\mathbf{G}\|_* + \mathbf{\Lambda}_1^{\mathrm{T}}(\mathbf{G}-\mathbf{\Theta}) + \frac{\mu}{2}\|\mathbf{G}-\mathbf{\Theta}\|_{\mathrm{F}}^2 \right\}, \tag{24}$$

which is solved via the Singular Value Thresholding (SVT) operator [32]:

- *Step 1:* Input a matrix $\mathbf{M}$ of rank r and consider the singular value decomposition (SVD):

$$\mathbf{M} = \mathbf{U}\mathbf{S}\mathbf{V}, \quad \mathbf{S} = \mathrm{diag}(\{s_k\}_{1\le k\le r}). \tag{25}$$

- *Step 2:* For each $\tau \ge 0$, we define the soft-thresholding operator $\mathcal{D}_\tau$ as follows

$$\mathcal{D}(\mathbf{M}) := \mathbf{U}\mathcal{D}_\tau(\mathbf{S})\mathbf{V}, \quad \mathcal{D}_\tau(\mathbf{S}) = \mathrm{diag}(\{s_k-\tau\}^+). \tag{26}$$

Using Eq. 26, $\|\mathbf{M}\|_*$ can be computed by $\|\mathcal{D}_\tau(\mathbf{S})\|_{1,1}$.

Optimization with respect to $\mathbf{H}$*:* The optimization problem of $\mathbf{H}$ is

$$\min_{\mathbf{H}} \left\{ \gamma\|\mathbf{H}\|_{1,1} + \mathbf{\Lambda}_2^{\mathrm{T}}(\mathbf{H}-\mathbf{X}) + \frac{\mu}{2}\|\mathbf{H}-\mathbf{X}\|_{\mathrm{F}}^2 \right\}, \tag{27}$$

its solution is nothing but a well-known *soft threshold* [17]:

$$\mathbf{H} \leftarrow \max\{\mathbf{0}, |\mathbf{X}-\mathbf{\Lambda}_2/\mu| - \gamma/\mu\} \odot \mathrm{sign}(\mathbf{X}-\mathbf{\Lambda}_2/\mu). \tag{28}$$

Optimization with respect to $\mathbf{J}$*:* The subproblem of $\mathbf{J}$ can be given by

$$\min_{\mathbf{J}} \left\{ \mathbf{\Lambda}_3^{\mathrm{T}}(\mathbf{J}-\mathbf{X}) + \frac{\mu}{2}\|\mathbf{J}-\mathbf{X}\|_{\mathrm{F}}^2 + l_R^+(\mathbf{J}) \right\}, \tag{29}$$

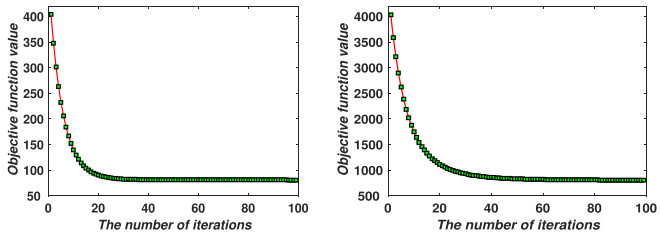

(a) Synthetic Data (b) Urban Data

Fig. 2. Convergence analysis of SULoRA are experimentally performed on a synthetic data and a real urban data.

$\mathbf{J}$ can be updated using the following rule

$$\mathbf{J} \leftarrow \max\{\mathbf{0}, \mathbf{X}-\mathbf{\Lambda}_3/\mu\}. \tag{30}$$

Lagrange multipliers update $\{\mathbf{\Lambda_i}\}_{i=1}^3$*:* In each iteration, Lagrange multipliers need to be updated by

$$\begin{aligned} & \mathbf{\Lambda}_1 \leftarrow \mathbf{\Lambda}_1 + \mu(\mathbf{G}-\mathbf{\Theta}),\ \mathbf{\Lambda}_2 \leftarrow \mathbf{\Lambda}_2 + \mu(\mathbf{H}-\mathbf{X}) \\ & \mathbf{\Lambda}_3 \leftarrow \mathbf{\Lambda}_3 + \mu(\mathbf{J}-\mathbf{X}). \end{aligned} \tag{31}$$

E. Convergence Analysis and Computational Cost

ADMM used in our optimization problem can be actually generalized to *inexact* Augmented Lagrange Multiplier (ALM) [33], whose convergence has been well studied when the number of block is less than three [29]. There is still not a *generally and strictly* theoretical proof in multi-blocks case. Fortunately for our case, its convergence is similarly guaranteed and supported in [32], [34]–[37]. Moreover, we experimentally record the objective function values in each iteration to draw the convergence curves of SULoRA on two used hyperspectral scenes (see Fig. 2).

As observed from Section III-D, the computational cost in the SULoRA algorithm is dominated by matrix products, and then the computational complexity of each subproblem in Eq. (18) with respect to the variables $\mathbf{X}$, $\mathbf{\Theta}$, $\mathbf{G}$, $\mathbf{H}$, and $\mathbf{J}$ are, in each iteration, $\mathcal{O}(D^2N)$, $\mathcal{O}(D^2N)$, $\mathcal{O}(D^3)$, $\mathcal{O}(PN)$, and $\mathcal{O}(PN)$, respectively, where the most costly step is solving $\mathbf{\Theta}$, hence yielding an overall $\mathcal{O}(D^2N)$ computational cost for Eq. (18).

IV. Experiments

In this section, we quantitatively and visually evaluate the unmixing performance of the proposed SULoRA on a synthetic dataset presented in [14] and two real datasets over the areas of Urban and MUFFLE Gulfport Campus, in comparison with eight classical and state-of-the-art methods, including FCLSU, PCLSU, SPCLSU, SUnSAL, SSUnSAL (scaled SUnSAL), SLRU (sparse and low-rank unmixing) [38], PLMM and ELMM. We experimentally and empirically choose the regularization parameters to maximize performance of above methods. To make fair visual comparisons, we fix a display range of the abundance maps from 0 to 1 in Figs. 4 and 9. Because there are some algorithms ignoring the effects of scaling factors, resulting in the abundances that show the maximum of the display range but actually exceed it.

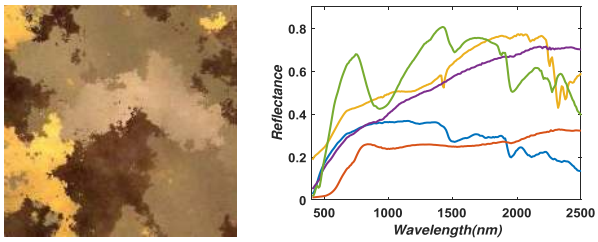

(a) A false color image (b) Endmembers

Fig. 3. A false color image of the synthetic data and corresponding five endmembers used for data simulation.

A. Synthetic Data

1) Data Description: Spectral simulation in the synthetic data is performed using five reference endmembers randomly selected from the spectral library of United States Geological Survey (USGS) with the size of 200 × 200 abundance maps generated using Gaussian fields, which strictly satisfies the abundance non-negative constraint (ANC) and the abundance sum-to-one constraint (ASC). The image consists of 200 × 200 pixels with 224 spectral bands in the wavelength from 400 nm to 2500 nm with spectral resolution. Fig. 3 shows a false color image of the synthetic data and five endmembers used for data simulation. The details of data simulation process can be unfolded as follows: Firstly, given five reference endmembers from USGS library, we multiply randomly-generated scaling factors ranging in [0.75, 1.25] by the spectral signatures, then a 25 dB white Gaussian noise was added to these scaled reference endmembers. Secondly, we linearly mix them with the generated abundance maps. Finally, an additive 25 dB white Gaussian was again added to the mixed spectrum. Using this simulation process, the spectral signature of each pixel in this dataset should be able to have a complex spectral variability consisting of endmember-dependent scaling factors and complex noise. Therefore, this simulated data with such spectral variability will give us a proper scenario to validate the proposed approach. More details for generating the simulated data can be found in [14].

2) Experimental Setup: Assuming the presence of pure endmembers in HSI scene, VCA, which is one of the most popular endmember extraction methods, is adopted in this paper to construct the endmember dictionary, while Hysime is used to estimate the number of endmembers. Next, these extracted endmembers can be effectively identified using the spectral angle compared to five reference endmembers.

To fairly assess the unmixing performance, we set the optimal parameters for the different algorithms. Both SUnSAL and SSUnSAL are parameterized by $2e-3$ on the sparsity-promoting term, while three regularization parameters [12] for abundances, endmembers, and perturbation in the PLMM are set to be $1e-2$, $1e-2$, and 1, respectively. The regularization parameter λ_S [14] in the ELMM is set to be 0.5. We also set the parameters of SLRU's sparse and low-rank terms to $2e-3$ and $1e-2$. α, β, and γ in Eqs. (16) and (17) can be set to 0.1, 0.01, and $8e-3$, respectively to maximize the performance of SULoRA.

Considering a fact that our method is an alternating minimizing optimization problem for multi-variables, a proper initialization would lead to a fast and reasonable solution. The abundance maps ($\mathbf{X}_0$) is initialized using the output of SPCLSU. Please refer to Algorithm 1 for more parameter settings.

We draw on three criteria of [14] to quantify the unmixing results, that is abundance overall root mean square error (aRMSE), reconstruction overall root mean square error (rRMSE), and average spectral angle mapper (aSAM). When the groundtruth of abundance maps ($\mathbf{X}^g = [\mathbf{x}_1^g, \ldots, \mathbf{x}_i^g, \ldots, \mathbf{x}_N^g] \in \mathbb{R}^{P\times N}$) is given, and then the estimated abundance maps ($\mathbf{X}^e = [\mathbf{x}_1^e, \ldots, \mathbf{x}_i^e, \ldots, \mathbf{x}_N^e] \in \mathbb{R}^{P\times N}$) can be measured by aRMSE defined as

$$aRMSE = \frac{1}{N}\sum_{i=1}^{N}\sqrt{\frac{1}{P}\sum\nolimits_{p=1}^{P}(\mathbf{x}_{pi}^e - \mathbf{x}_{pi}^g)^2}. \tag{32}$$

If without the reference of abundance maps, the other two rules (rRMSE and aSAM) are used by computing reconstruction errors between the observed hyperspectral data $\mathbf{Y}^o = [\mathbf{y}_1^o, \ldots, \mathbf{y}_i^o, \ldots, \mathbf{y}_N^o] \in \mathbb{R}^{D\times N}$ and its reconstruction $\mathbf{Y}^r = [\mathbf{y}_1^r, \ldots, \mathbf{y}_i^r, \ldots, \mathbf{y}_N^r] \in \mathbb{R}^{D\times N}$. The former is defined by

$$rRMSE = \frac{1}{N}\sum_{i=1}^{N}\sqrt{\frac{1}{D}\sum\nolimits_{l=1}^{D}(\mathbf{y}_{di}^r - \mathbf{y}_{di}^o)^2}, \tag{33}$$

while the latter is aSAM, expressed as

$$aSAM = \frac{1}{N}\sum_{k=1}^{N} arccos\left(\frac{\mathbf{y}_i^{r\mathrm{T}}\mathbf{y}_i^o}{\|\mathbf{y}_i^r\|\|\mathbf{y}_i^o\|}\right). \tag{34}$$

For a fair and reasonable comparison, we average the results of the three criteria out of 10 runs for the different algorithms, because VCA cannot always guarantee the same estimations in each round.

3) Results and Discussion: Fig. 4 shows the estimated abundance maps of the different algorithms, while Table I correspondingly lists the quantitative assessment for three different indices (aRMSE, rRMSE, and aSAM) and computational cost for each algorithm. Since the visual difference of Fig. 4 is not salient, we highlight the differences by the abundance difference maps displayed in Fig. 5.

Visually, FCLSU and PLMM yield a poor performance due to the presence of the spectral variability in the simulated scene. More precisely, the abundance maps estimated by FCLSU fully absorb the spectral variabilities, attributing to the sum-to-one constraint. Taking the rest of algorithms by and large, those of modeling scaling factors outperform those without considering ones. A similar quantitative trend also can be found in Table I. In details, the performance of PCLSU is better than that of FCLSU, since the PCLSU's abundances can be reasonably estimated in a cone not in a simplex by dropping the ASC. Actually the spectral variability is not eliminated by PCLSU, but still partially absorbed by the abundances. Fig. 4 provides a convincing evidence that the abundances for some pixels are higher than 1, and this violates the ASC. By trickily alleviating the effects of scaling factors, the abundances estimated by SPCLSU are more accurate than PCLSU's. Putting the sparse prior on the

TABLE I
THE QUANTITATIVE COMPARISON OF UNMIXING PERFORMANCE FOR THE DIFFERENT ALGORITHMS ON THE SYNTHETIC DATA. THE BEST ONE IS MARKED IN BOLD

Algorithm	FCLSU	PCLSU	SUnSAL	SPCLSU	SSUnSAL	SLRU	PLMM	ELMM	SURoLA
aRMSE	0.0630	0.0421	0.0399	0.0263	0.0243	0.0239	0.0621	0.0323	**0.0220**
rRMSE	0.0150	0.0123	0.0123	0.0123	0.0123	0.0123	0.0129	0.0058	**0.0011**
aSAM	1.9836	1.7717	1.7726	1.7717	1.7726	1.7712	1.8427	0.8392	**0.1789**
$\mathcal{O}$	DPN	DPN	DPN	DPN	DPN	DPN	DP^2N	DP^2N	D^2N

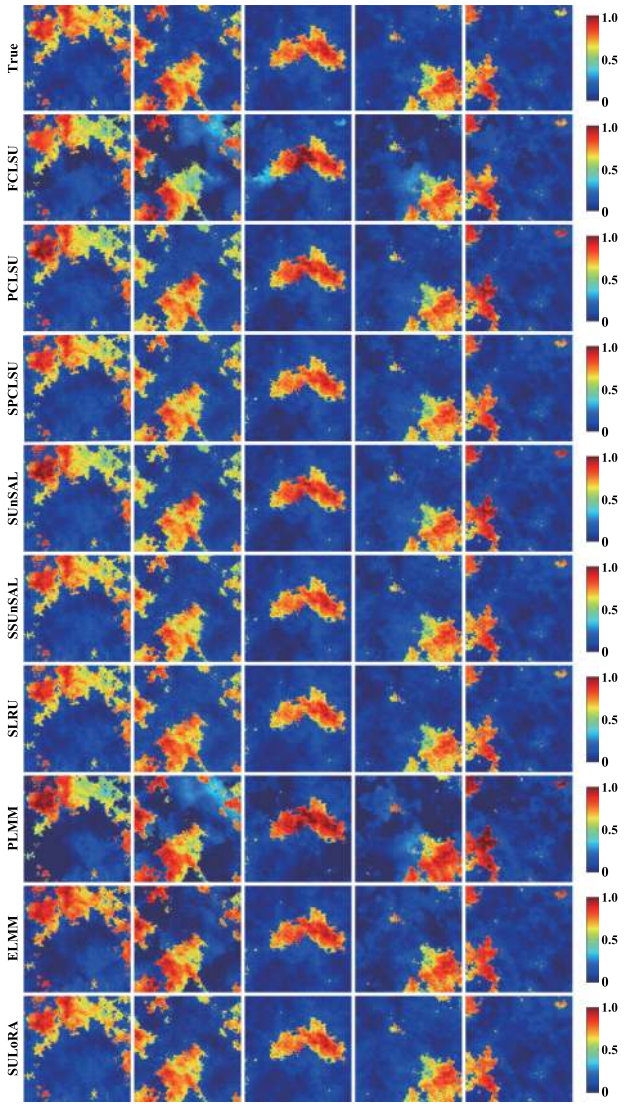

Fig. 4. Abundances estimated by different SU methods (each column corresponds to one endmember extracted by VCA) and the first row shows the ground truth.

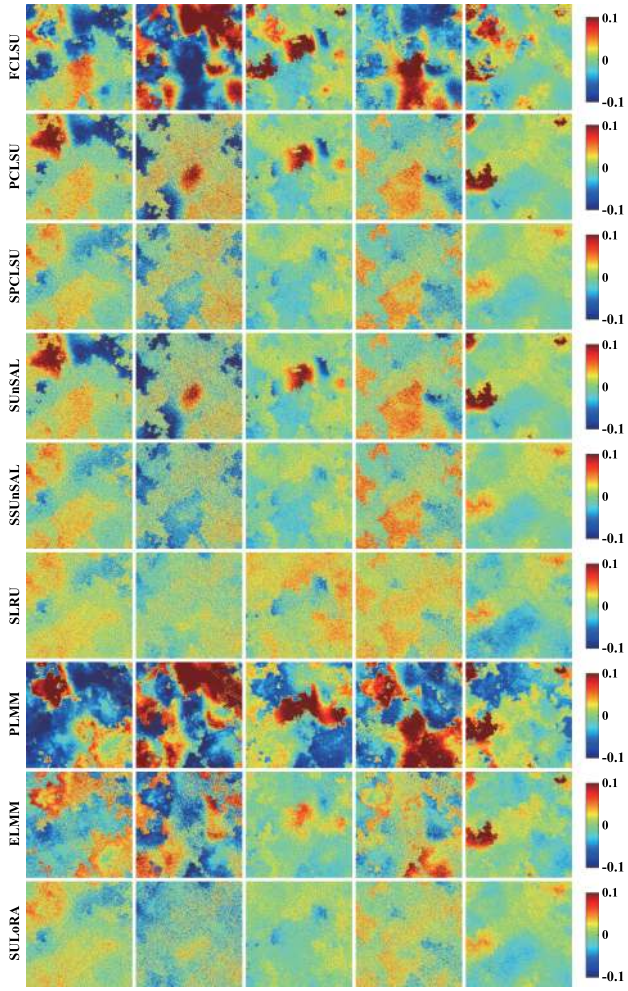

Fig. 5. Difference abundance maps using different spectral unmixing methods corresponding to Fig. 4.

abundance maps, SUnSAL and its scaled version (SSUnSAL) can further improve the performance compared to those without the sparsity-promoting term. This indirectly demonstrates that each pixel in HSI is composed of a few materials. In SLRU, the abundance maps are simultaneously constrained to be sparse and low-rank, leading to a slight improvement compared to only sparsity-promoting SUnSAL algorithm.

The ability in handling the other spectral variability that scaling factors can not be explained limits the ELMM. Furthermore, ELMM needs to simultaneously estimate a coupled set of variables (the scaling factors and abundance maps), this leads to a non-convex optimization problem, which easily drops to a local minimum. In a local region of HSI, the scaling factors for the different endmembers are highly correlated, because the endmember variability is dominated by the topography structure. This is possibly another factor that hinders the performance of the ELMM improving. For the PLMM, it attempts to model the spectral variabilities in a general way, but only a perturbed

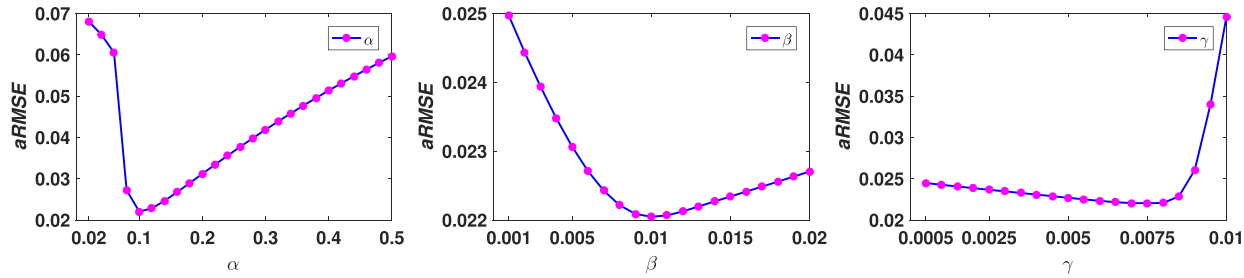

Fig. 6. Sensitivity analysis of three regularization parameters (e.g., α, β, and γ) in SULoRA (Eq. 18).

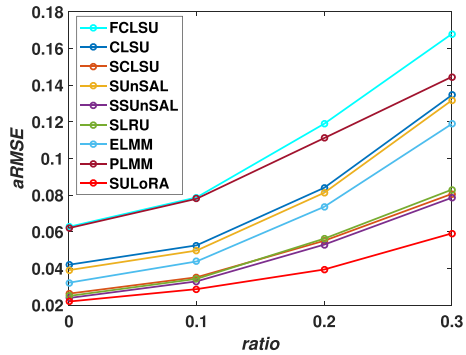

Fig. 7. Robustness evaluation of these compared algorithms using a RMSE at the different sparse noise ratio.

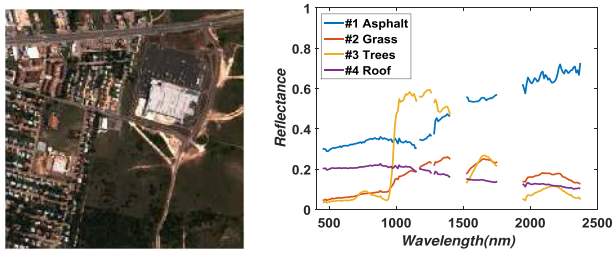

(a) A false color image (b) Endmembers

Fig. 8. A false color image of the Urban data and four extracted endmembers used in spectral unmixing.

information assumed by a Gaussian prior fails to represent the spectral variability (e.g. scaling factors).

As expected, the performance of the subspace-based spectral unmixing (the proposed SULoRA) is superior to that of other algorithms unmixing in the original hyperspectral space, indicating its superiority and effectiveness in dealing with the spectral variability. Fig. 5 highlights a more significant comparison using abundance difference maps between the groundtruth and the estimated abundance maps, where there are lower difference values in SULoRA than in others.

4) Parameters Sensitivity Analysis: The performance of the proposed SULoRA algorithm in Eq. (18) is, to some extent, sensitive to the setting of three regularization parameters (α, β, and γ), it is, as a result, indispensable to search a set of optimal parameter combination. For this reason, the corresponding experiments are conducted to investigate the parameters effects on the performance of estimating abundance maps (measured by aRMSE), as specifically shown in Fig. 6 where the optimal parameter combination in SULoRA is $\alpha = 0.1$, $\beta = 0.01$, and $\gamma = 8e-3$, respectively.

5) Robustness Analysis to Sparse Noise: We further investigate the robustness of the SULoRA against *sparse noise*. For this purpose, the simulated data is corrupted by sparse noise with different corrupted levels, namely $ratio = 0, 0.1, 0.2, 0.3$, where $ratio = 0$ denotes no additional sparse noise is added to the simulated data while $ratio = 0.1$, for instance, means that the 10% of total pixels are corrupted by additional sparse noise. Please refer to [39]–[41] for more experimental setting. As can be seen from Fig. 7, with the increase of *sparse noise ratio*, the performance of most compared approaches dramatically degrades, yet SULoRA still holds a stable and robust performance.

B. Real Data Over Urban Area

1) Data Description: This dataset was acquired by the Hyperspectral Digital Imagery Collection Experiment (HYDICE) over an urban area of Copperas Cove, Texas, USA. The entire image consists of 307×307 pixels at a ground sampling distance (GSD) of 2 m, and 58 noisy bands are removed, so that a total of 162 bands covering the spectral rank from 400 nm to 2500 nm with spectral resolution of 10 nm is selected by removing 58 noisy bands corrupted by water absorption and atmospheric effects in our experiments. This dataset used in hyperspectral unmixing has been widely reported in [42]–[44]. Additionally, we use a latest data version issued by Geospatial Research Laboratory (USA) and Engineer Research and Development Center (USA) in 2015.[1] Fig. 8(a) shows a false color image of the study scene and the endmembers are extracted by VCA.

2) Experimental Setup: There are four main endmembers in the scene: asphalt (road and parking lot), grass, trees, and roof. Please see the references [42] and [44] for more details. Similarly to the first data, HySime and VCA are adopted to determine the number of endmembers and extract the endmembers, respectively. Fig. 8(b) shows the endmembers used in spectral unmixing. The endmembers can be simply identified by comparing with the reference endmembers.[2]

According to two indices of aRMSE and aSAM, we select the optimal parameters for these compared algorithms. The parameters for the sparse and low-rank regularization terms in SLRU are set to $1e-2$ and $1e-2$. The sparsity-promoting term in SUnSAL and SSUnSAL is penalized by $6e-3$, while for PLMM, three regularization parameters for abundances, endmembers,

[1] http://www.tec.army.mil/Hypercube

[2] The reference endmembers can be introduced in [44] and [43].

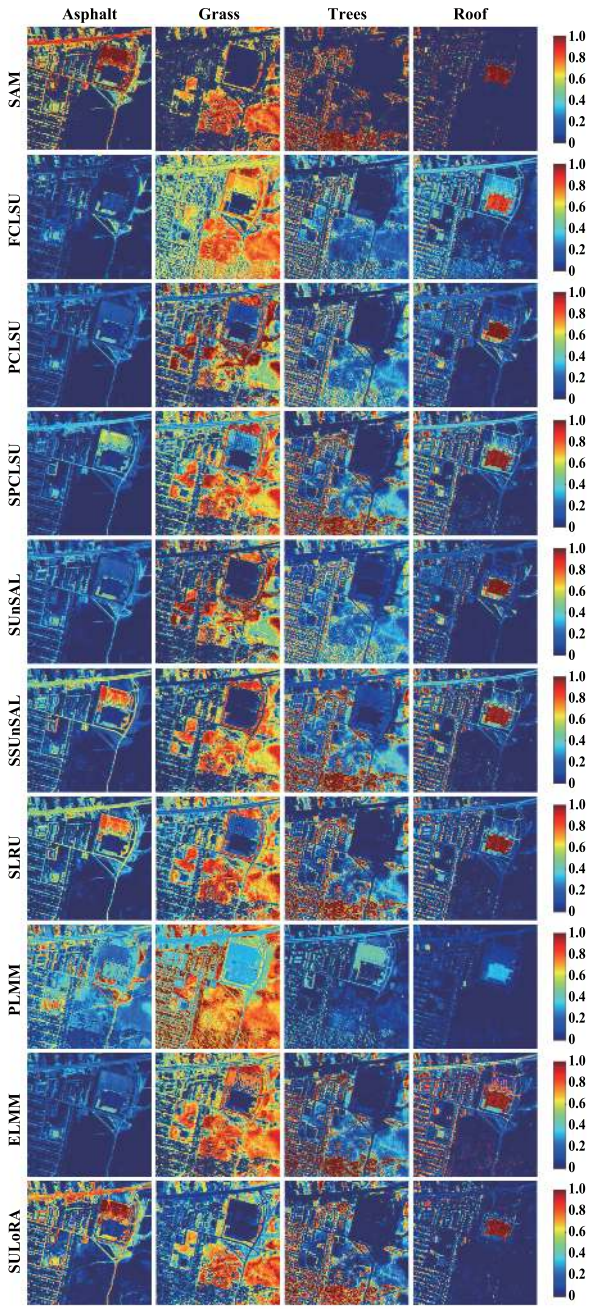

Fig. 9. Abundance maps comparison between the proposed method and the state-of-art methods.

and perturbation are selected to be $1e-2$, $1e-3$, and 1, respectively. The balance parameter λ_S in the ELMM is still 0.5. We finely tune α, β, and γ in SULoRA to 0.1, 0.01, and $5e-3$, respectively.

3) Results and Analysis: As there are no references of the abundance maps for the urban dataset, we propose to apply classification maps, i.e. overall accuracy (OA), to approximately assess the abundance maps. By comparing with the reference endmembers, the spectral angle mapper (SAM) is used to roughly generate classification results, as shown in the first row of Fig. 9 where the positive samples are marked in cosine similarity, while negative samples are masked out with 0. More specifically, we classify each pixel into an endmember with a maximum abundance response. As a result, OA can be regarded as a new index for evaluating the different methods, as listed in Table II. FCLSU performs a worse estimation in the abundances compared to other algorithms, since a more complex spectral variability comes into play in the real data. PCLSU sill fails to well deal with such spectral variability, despite a better performance than FCLSU. As visually shown in the Fig. 9, SPCLSU can effectively identify the materials of asphalt, trees, and roof, while considering scaling factors. As a comparison, neither FCLSU nor PCLSU detects the material of the asphalt, but SPCLSU successfully does. The regular pattern is also applicable to SUnSAL and SSUnSAL. By additionally considering a low-rank prior in the process of estimating abundance maps, SLRU performs better than SUnSAL, but it still fails to address the complex spectral variability.

Although ELMM is able to detect some areas, e.g. trees and roof, the complex spectral variability in the real scenario can not be fully interpreted only by scaling factors. This results in a relatively lower rRMSE and aSAM, as listed in Table II. On the other hand, the hard optimization problem in ELMM is another drawback, limiting ELMM up to a better performance. The main factor for the poor performance of PLMM is lack of a powerful fitting ability in the spectral variability by analyzing the visual and quantitative results from both Fig. 9 and Table II.

Thanks to the high-resolution of the urban HSI, we can find many pure pixels, but they are mistaken as mixed pixels with the existence of spectral variability. This easily makes many pixels misclassified using the aforementioned methods. Different with them, SULoRA can estimate the abundance maps in a robust subspace, so that its visual effect is superior to others', as shown in Fig. 9, and a consistent numerical evaluation is also listed in Table II. For instance, the asphalt and grass can be purely identified by SULoRA, unlike the others. The abundance maps of the tree and roof estimated by SULoRA show higher contrast as well. These phenomena can objectively explain the robustness and effectiveness of the proposed method.

C. Real Data (MUUFL Gulfport Campus)

1) Data Description: As introduced in [45], [46], the labeled hyperspectral image can be used for ultimately assessing the unmixing performance, hence the MUUFL Gulfport dataset is chosen as the second real data in our case, collected over the campus area in University of Southern Mississippi-Gulfpark Campus, Long Beach, Mississippi, USA [47]. It consists of 325×220 pixels at a GDS of 1 m. There are 11 classes in this study scene, but we just consider 8 main classes as they have enough number of pixels and clear spatial structure for a easier visualization, that is *#1 trees*, *#2 mostly-grass ground surface*, *#3 mixed ground surface*, *#4 dirt and sand*, *#5 road*, *#6 buildings*, *#7 shadow of buildings*, and *#8 sidewalk*. The 8 noisy bands were removed, resulting in a total of 64 bands left in the spectral range from 375 nm to 1050 nm. Fig. 10 shows a RGB image and the endmembers extracted by VCA of the used scene.

TABLE II
THE QUANTITATIVE COMPARISON OF UNMIXING PERFORMANCE FOR THE DIFFERENT ALGORITHMS ON THE REAL URBAN DATA. THE BEST ONE IS MARKED IN BOLD

Algorithm	FCLSU	PCLSU	SUnSAL	SPCLSU	SSUnSAL	SLRU	PLMM	ELMM	SULoRA
OA (%)	54.66	68.08	71.26	68.08	71.26	73.59	58.55	62.41	**86.71**
rRMSE	0.0397	0.0086	0.0086	0.0086	0.0086	0.0084	0.0111	0.0072	**0.0019**
aSAM	8.6734	2.9569	2.9582	2.9569	2.9582	2.9472	3.6240	2.0378	**0.6491**

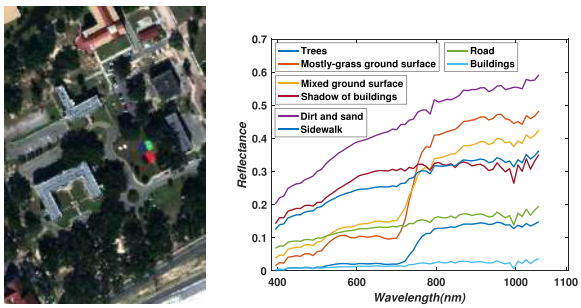

(a) A false color image (b) Endmembers

Fig. 10. A RGB image of the MUFFLE dataset and eight extracted endmembers used in spectral unmixing.

2) Experimental Setup: Likewise, the number of endmembers can be estimated by HySime and the endmembers can be extracted by VCA. The extracted endmembers are handily identified using SAM, as massive labeled samples for each class are available.

The optimal parameters for all compared methods and the proposed SULoRA are detailed in the following. The l_1-norm term in SUnSAL and SSUnSAL is parameterized by $3e-4$, while the parameters for SLRU are $2e-4$ and 0.1, respectively. Three regularization parameters in PLMM are set to be $1e-3$, $1e-2$, and 1, respectively, while the parameter λ_S in ELMM plays a role in balancing the two fidelity terms, which is assigned to 0.5 in our case. For SULoRA, α, β, and γ are experimentally assigned to 0.8, 0.1, and $6e-4$, respectively.

3) Results and Analysis: Given these labeled classification maps of each class as shown in the first row of Fig. 11, classification (e.g., OA) can be explored as a potential way to evaluate the quality of estimated abundance maps. Correspondingly, Table III quantitatively lists the performance assessment (three indices: OA, rRMSE, and aSAM) for all algorithms.

FCLSU shows a poor estimation in abundance maps, since it fails to model the complex spectral variabilities. For those algorithms that provide different priors in estimating the abundance maps, e.g., scaling (SPCLSU, SSUnSAL), sparse (SUnSAL, SSUnSAL), low-rank (SLRU), etc., there is a moderate performance improvement compared to those without considering prior knowledge. One thing to be noted is that PLMM obtains desirable results of rRMSE and aSAM in comparison with previous methods (expect our proposed SULoRA), but interestingly it yields a poorest OA. The reason for this mainly lies in that only perturbation information hardly represents the complex spectral variability, and meanwhile such modeling strategy could also corrupt some important spectral attributes misdeemed as certain

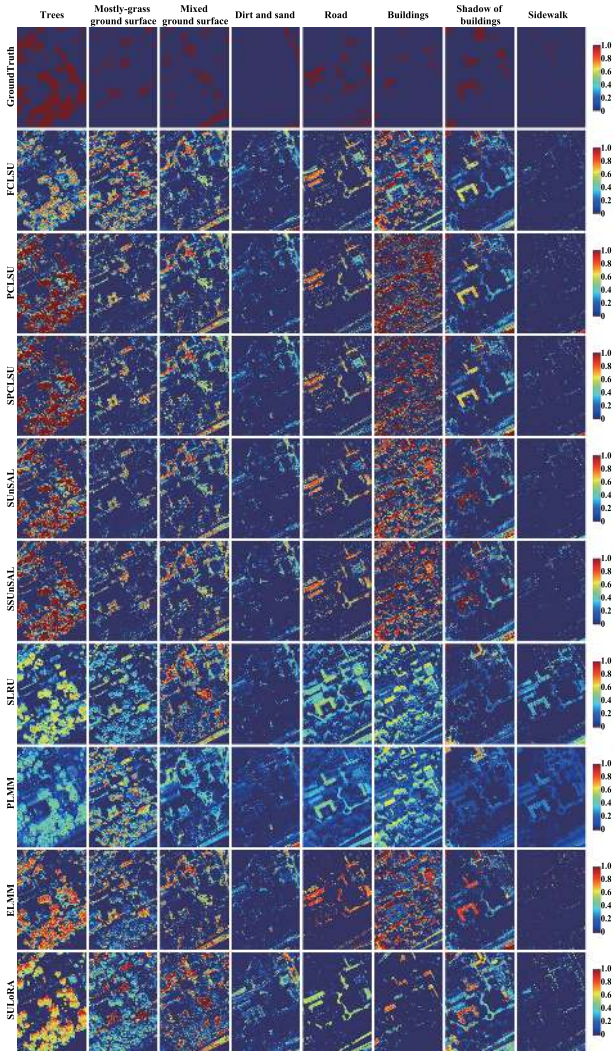

Fig. 11. Abundance maps comparison between the proposed method and the state-of-art methods.

spectral variability. As can be seen from Fig. 11, ELMM obtains a good abundance estimation, since it is good at handling the scaling factors (principle spectral variability). But unfortunately, ELMM's performance is limited by the presence of other spectral variabilities. In a word, these previously proposed methods basically pay more attentions on somewhat special spectral variability, lacking of generalization ability. Considering the complexity of the spectral variability in real-world, the proposed SULoRA accounts for spectral variability in a generalized fashion by embedding the low-rank attribute, resulting in more robust

TABLE III
THE QUANTITATIVE COMPARISON OF UNMIXING PERFORMANCE FOR THE DIFFERENT ALGORITHMS ON THE MUFFLE GULFPORT CAMPUS DATA. THE BEST ONE IS MARKED IN BOLD

Algorithm	FCLSU	PCLSU	SUnSAL	SPCLSU	SSUnSAL	SLRU	PLMM	ELMM	SULoRA
OA (%)	55.52	62.21	66.61	62.21	66.61	66.58	51.65	63.16	**85.86**
rRMSE	0.0135	0.0110	0.0109	0.0110	0.0109	0.0162	0.0099	0.0127	**0.0058**
aSAM	5.5854	4.7699	4.7830	4.7699	4.7830	6.6452	4.0436	5.1839	**2.6003**

and effective unmixing results visually and quantitatively (see Fig. 11).

V. CONCLUSION

This paper is motivated by the fact that the spectral signature in the original hyperspectral space inevitably suffers from largely and diversely spectral variabilities. To address this issue, we propose to unmix the HSI in a subspace instead of in the original space. This results in a general subspace unmixing framework that jointly learns a subspace projection and abundance maps. With the low-rank attribute embedding, we further develop a low-rank subspace unmixing approach, called **s**pectral **u**nmixing with **lo**w-**r**ank **a**ttribute embedding (SULoRA). Experimental results demonstrate that SULoRA is able to obtain a higher unmixing performance both visually and quantitatively, than other state-of-the-art algorithms. In the future, we would like to cast the subspace-based framework to advanced unmxing methods designed in the original spectral space, aiming at a more robust spectral unmixing.

ACKNOWLEDGMENT

The authors would like to thank P.-A. Thouvenin from Institut de Recherche en Informatique de Toulouse and Prof. J. M. Bioucas-Dias for providing MATLAB codes with respect to PLMM and SUnSAL tested in their experiments, and the Hyperspectral Digital Imagery Collection Experiment for sharing the urban dataset free of charge. The authors would like to express their appreciation to Prof. J. Chanussot for providing the simulated dataset used in their first experiment as well as MATLAB codes for ELMM.

REFERENCES

[1] D. Hong, N. Yokoya, and X. Zhu, "Learning a robust local manifold representation for hyperspectral dimensionality reduction," *IEEE J. Sel. Topics Appl. Earth Observ. Remote Sens.*, vol. 10, no. 6, pp. 2960–2975, Jul. 2017.

[2] D. Hong, N. Yokoya, J. Xu, and X. Zhu, "Joint & progressive learning from high-dimensional data for multi-label classification," in *Proc. Eur. Conf. Comput. Vis.*, 2018, pp. 469–484.

[3] M. Veganzones, G. Tochon, M. Dalla-Mura, A. Plaza, and J. Chanussot, "Hyperspectral image segmentation using a new spectral unmixing-based binary partition tree representation," *IEEE Trans. Image Process.*, vol. 23, no. 8, pp. 3574–3589, Aug. 2014.

[4] T. Matsuki, N. Yokoya, and A. Iwasaki, "Hyperspectral tree species classification of Japanese complex mixed forest with the aid of lidar data," *IEEE J. Sel. Topics Appl. Earth Observ. Remote Sens.*, vol. 8, no. 5, pp. 2177–2187, Apr. 2015.

[5] Z. Wang, R. Zhu, K. Fukui, and J. Xue, "Matched shrunken cone detector (MSCD): Bayesian derivations and case studies for hyperspectral target detection," *IEEE Trans. Image Process.*, vol. 26, no. 11, pp. 5447–5461, Aug. 2017.

[6] D. A. Roberts, M. Gardner, R. Church, S. Ustin, G. Scheer, and R. O. Green, "Mapping chaparral in the Santa Monica mountains using multiple endmember spectral mixture models," *Remote Sens. Environ.*, vol. 65, no. 3, pp. 267–279, 1998.

[7] C. Yang, J. H. Everitt, Q. Du, B. Luo, and J. Chanussot, "Using high-resolution airborne and satellite imagery to assess crop growth and yield variability for precision agriculture," *Proc. IEEE*, vol. 101, no. 3, pp. 582–592, Jul. 2013.

[8] J. M. Bioucas-Dias *et al.*, "Hyperspectral unmixing overview: Geometrical, statistical, and sparse regression-based approaches," *IEEE J. Sel. Topics Appl. Earth Observ. Remote Sens.*, vol. 5, no. 2, pp. 354–379, Feb. 2012.

[9] A. Zare and K. Ho, "Endmember variability in hyperspectral analysis: Addressing spectral variability during spectral unmixing," *IEEE Signal Process. Mag.*, vol. 31, no. 1, pp. 95–104, Dec. 2014.

[10] O. Eches, N. Dobigeon, C. Mailhes, and J.Y. Tourneret, "Bayesian estimation of linear mixtures using the normal compositional model," *IEEE Trans. Image Process.*, vol. 19, no. 6, pp. 1403–1413, Jun. 2010.

[11] X. Du, A. Zare, P. Gader, and D. Dranishnikov, "Spatial and spectral unmixing using the beta compositional model," *IEEE J. Sel. Topics Appl. Earth Observ. Remote Sens.*, vol. 7, no. 6, pp. 1944–2003, Jun. 2014.

[12] P. A. Thouvenin, N. Dobigeon, and J. Y. Tourneret, "Hyperspectral unmixing with spectral variability using a perturbed linear mixing model," *IEEE Trans. Signal Process.*, vol. 64, no. 2, pp. 525–538, Jun. 2016.

[13] X. Fu, W. K. Ma, J. M. Bioucas-Dias, and T. H. Chan, "Semiblind hyperspectral unmixing in the presence of spectral library mismatches," *IEEE Trans. Geosci. Remote Sens.*, vol. 54, no. 9, pp. 5171–5184, May 2016.

[14] L. Drumetz, M. A. Veganzones, S. Henrot, R. Phlypo, J. Chanussot, and C. Jutten, "Blind hyperspectral unmixing using an extended linear mixing model to address spectral variability," *IEEE Trans. Image Process.*, vol. 25, no. 8, pp. 3890–3905, Aug. 2016.

[15] D. C. Heinz and C. I. Chang, "Fully constrained least squares linear spectral mixture analysis method for material quantification in hyperspectral imagery," *IEEE Trans. Geosci. Remote Sens.*, vol. 39, no. 3, pp. 529–545, Mar. 2001.

[16] R. Heylen, D. Burazerovic, and P. Scheunders, "Fully constrained least squares spectral unmixing by simplex projection," *IEEE Trans. Geosci. Remote Sens.*, vol. 49, no. 11, pp. 4112–4122, Nov. 2011.

[17] J. M. Bioucas-Dias and M. Figueiredo, "Alternating direction algorithms for constrained sparse regression: Application to hyperspectral unmixing," in *Proc. IEEE Workshop Hyperspectral Image Signal Process., Evol. Remote Sens.*, 2010, pp. 1–4.

[18] M. A. Veganzones *et al.*, "A new extended linear mixing model to address spectral variability," in *Proc. IEEE Workshop Hyperspectral Image Signal Process., Evol. Remote Sens.*, 2014, pp. 1–5.

[19] D. Hong, N. Yokoya, J. Chanussot, and X. Zhu, "Learning low-coherence dictionary to address spectral variability for hyperspectral unmixing," in *Proc. IEEE Int. Conf. Image Process.*, Beijing, China, Sep. 2017, pp. 235–239.

[20] J. M. P. Nascimento and J. M. Bioucas-Dias, "Vertex component analysis: A fast algorithm to unmix hyperspectral data," *IEEE Trans. Geosci. Remote Sens.*, vol. 43, no. 4, pp. 898–910, Apr. 2005.

[21] M. D. Iordache, J. M. Bioucas-Dias, and A. Plaza, "Total variation spatial regularization for sparse hyperspectral unmixing," *IEEE Trans. Geosci. Remote Sens.*, vol. 50, no. 11, pp. 4484–4502, Nov. 2012.

[22] M. D. Iordache, J. M. Bioucas-Dias, and A. Plaza, "Collaborative sparse regression for hyperspectral unmixing," *IEEE Trans. Geosci. Remote Sens.*, vol. 52, no. 1, pp. 341–354, Jan. 2014.

[23] H. Kim and H. Park, "Nonnegative matrix factorization based on alternating nonnegativity constrained least squares and active set method," *SIAM. J. Matrix Anal. Appl.*, vol. 30, no. 2, pp. 713–730, Jul. 2008.

[24] C. Su, F. Yang, S. Zhang, Q. Tian, L. S. Davis, and W. Gao, "Multi-task learning with low rank attribute embedding for person re-identification," in *Proc. IEEE Int. Conf. Comput. Vis.*, 2015, pp. 3739–3747.

[25] E. Elhamifar and R. Vidal, "Sparse subspace clustering: Algorithm, theory, and applications," *IEEE Trans. Pattern Anal. Mach. Intell.*, vol. 35, no. 11, pp. 2765–2781, Nov. 2013.
[26] N. Shahid, N. Perraudin, V. Kalofolias, G. Puy, and V. P. Andergheynst, "Fast robust PCA on graphs," *IEEE J. Sel. Topics Signal Process.*, vol. 10, no. 4, pp. 740–756, Jun. 2016.
[27] L. Zhang, W. Wei, Y. Zhang, C. Shen, A. van den Hengel, and Q. Shi, "Cluster sparsity field: An internal hyperspectral imagery prior for reconstruction," *Int. J. Comput. Vis.*, vol. 126, pp. 797–821, 2018.
[28] J. M. Bioucas-Dias and J. M. P. Nascimento, "Hyperspectral subspace identification," *IEEE Trans. Geosci. Remote Sens.*, vol. 46, no. 8, pp. 2435–2445, Jul. 2008.
[29] Z. Lin, M. Chen, and Y. Ma, "The augmented lagrange multiplier method for exact recovery of corrupted low-rank matrices," 2010, arXiv:1009.5055.
[30] Z. Lin, R. Liu, and Z. Su, "Linearized alternating direction method with adaptive penalty for low-rank representation," in *Proc. Adv. Neural Inf. Process. Syst.*, 2011, pp. 612–620.
[31] L. Yang *et al.*, "Image reconstruction via manifold constrained convolutional sparse coding for image sets," *IEEE J. Sel. Topics Signal Process.*, vol. 11, no. 7, pp. 1072–1081, Oct. 2017.
[32] G. Liu, Z. Lin, S. Yan, J. Sun, Y. Yu, and Y. Ma, "Robust recovery of subspace structures by low-rank representation," *IEEE Trans. Pattern Anal. Mach. Intell.*, vol. 35, no. 1, pp. 171–184, Apr. 2013.
[33] L. Chen, X. Li, D. Sun, and K. Toh, "On the equivalence of inexact proximal ALM and ADMM for a class of convex composite programming," 2018, arXiv:1803.10803.
[34] Y. Xu, W. Yin, Z. Wen, and Y. Zhang, "An alternating direction algorithm for matrix completion with nonnegative factors," *Frontiers Math. China*, vol. 7, no. 2, pp. 365–384, Apr. 2012.
[35] Y. Zhang, Z. Jiang, and L. Davi, "Learning structured low-rank representations for image classification," in *Proc. IEEE Conf. Comput. Vis. Pattern Recognit.*, 2013, pp. 676–683.
[36] D. Fortun, P. Guichard, N. Chu, and M. Unser, "Reconstruction from multiple poses in fluorescence imaging: Proof of concept," *IEEE J. Sel. Topics Signal Process.*, vol. 10, no. 1, pp. 61–70, Feb. 2016.
[37] M. A. Davenport and J. Romberg, "An overview of low-rank matrix recovery from incomplete observations," *IEEE J. Sel. Topics Signal Process.*, vol. 10, no. 4, pp. 608–622, Jun. 2016.
[38] P. V. Giampouras, K. E. Themelisand A. A. Rontogiannis, and K. D. Koutroumbas, "Simultaneously sparse and low-rank abundance matrix estimation for hyperspectral image unmixing," *IEEE Trans. Geosci. Remote Sens.*, vol. 54, no. 8, pp. 4775–4789, Aug. 2016.
[39] W. He, H. Zhang, and L. Zhang, "Sparsity-regularized robust non-negative matrix factorization for hyperspectral unmixing," *IEEE J. Sel. Topics Appl. Earth Observ. Remote Sens.*, vol. 9, no. 9, pp. 4267–4279, Sep. 2016.
[40] Y. Chen, Y. Guo, Y. Wang, D. Wang, C. Peng, and G. He, "Denoising of hyperspectral images using nonconvex low rank matrix approximation," *IEEE Trans. Geosci. Remote Sens.*, vol. 55, no. 9, pp. 5366–5380, Sep. 2017.
[41] W. He, H. Zhang, H. Shen, and L. Zhang, "Hyperspectral image denoising using local low-rank matrix recovery and global spatial–spectral total variation," *IEEE J. Sel. Topics Appl. Earth Observ. Remote Sens.*, vol. 11, no. 3, pp. 713–729, Mar. 2018.
[42] F. Zhu, Y. Wang, S. Xiang, B. Fan, and C. Pan, "Structured sparse NMF for hyperspectral unmixing," *ISPRS J. Photogramm. Remote Sens.*, vol. 88, no. 1, pp. 101–118, Feb. 2014.
[43] Y. Wang, C. Pan, S. Xiang, and F. Zhu, "Robust hyperspectral unmixing with correntropy based metric," *IEEE Trans. Image Process.*, vol. 24, no. 11, pp. 4027–4040, Jul. 2015.
[44] X. Liu, W. Xia, B. Wang, and L. Zhang, "An approach based on constrained nonnegative matrix factorization to unmix hyperspectral data," *IEEE Trans. Geosci. Remote Sens.*, vol. 49, no. 2, pp. 757–772, Feb. 2011.
[45] G. Mountrakis, J. Im, and C. Ogole, "Support vector machines in remote sensing: A review," *ISPRS J. Photogramm. Remote Sens.*, vol. 66, no. 3, pp. 247–259, 2011.
[46] K. Makantasis, K. Karantzalos, A. Doulamis, and N. Doulamis, "Deep supervised learning for hyperspectral data classification through convolutional neural networks," in *Proc. IEEE Int. Geosci. Remote Sens. Symp.*, 2015, pp. 4959–4962.
[47] X. Du and A. Zare, "Technical report: Scene label ground truth map for MUUFL Gulfport data set," Univ. Florida, Gainesville, FL, USA, Tech. Rep. 20170417, Apr. 2017.

Danfeng Hong (S'16) received the B.Sc. degree in computer science and technology from Northeastern University, Shenyang, China, in 2012, and the M.Sc. degree in computer vision from Qingdao University, Qingdao, China, in 2015. He is currently working toward the Ph.D. degree with the Signal Processing in Earth Observation, Technical University of Munich, Munich, Germany, and the Remote Sensing Technology Institute, German Aerospace Center (DLR), Wessling , Germany. His research interests include image processing, pattern recognition, and machine learning and their applications to hyperspectral data analysis.

Xiao Xiang Zhu (S'10–M'12–SM'14) received the M.Sc., Dr.-Ing., and Habilitation degrees in signal processing from Technical University of Munich, Munich, Germany, in 2008, 2011, and 2013, respectively.

She is currently a Professor with the Signal Processing in Earth Observation (www.sipeo.bgu.tum.de) at Technical University of Munich, Munich, Germany, and German Aerospace Center (DLR), Wessling, Germany, the head of the department "EO Data Science" at DLR's Earth Observation Center, and the head of the Helmholtz Young Investigator Group "SiPEO" at DLR and TUM. He was a Guest Scientist or visiting professor with the Italian National Research Council (CNR-IREA), Naples, Italy, Fudan University, Shanghai, China, The University of Tokyo, Tokyo, Japan, and University of California, Los Angeles, CA, USA, in 2009, 2014, 2015, and 2016, respectively. Her main research interests are remote sensing and earth observation, signal processing, machine learning, and data science, with a special application focus on global urban mapping.

Dr. Zhu is a member of young academy (Junge Akademie/Junges Kolleg) at the Berlin-Brandenburg Academy of Sciences and Humanities and the German National Academy of Sciences Leopoldina and the Bavarian Academy of Sciences and Humanities. She is an Associate Editor for the IEEE TRANSACTIONS ON GEOSCIENCE AND REMOTE SENSING.